J. Fluid Mech. (2009), *vol.* 619, *pp.* 213–233.
doi:10.1017/S0022112008004618 Printed in the United Kingdom

Turbulent dynamics of pipe flow captured in a reduced model: puff relaminarization and localized 'edge' states

ASHLEY P. WILLIS[1]† AND RICH R. KERSWELL
School of Mathematics, University of Bristol, BS8 1TW Bristol, UK

(Received 17 December 2007 and in revised form 12 October 2008)

Fully three-dimensional computations of flow through a long pipe demand a huge number of degrees of freedom, making it very expensive to explore parameter space and difficult to isolate the structure of the underlying dynamics. We therefore introduce a '$2+\epsilon$-dimensional' model of pipe flow, which is a minimal three-dimensionalization of the axisymmetric case: only sinusoidal variation in azimuth plus azimuthal shifts are retained; yet the same dynamics familiar from experiments are found. In particular the model retains the subcritical dynamics of fully resolved pipe flow, capturing realistic localized 'puff-like' structures which can decay abruptly after long times, as well as global 'slug' turbulence. Relaminarization statistics of puffs reproduce the memoryless feature of pipe flow and indicate the existence of a Reynolds number about which lifetimes diverge rapidly, provided that the pipe is sufficiently long. Exponential divergence of the lifetime is prevalent in shorter periodic domains. In a short pipe, exact travelling-wave solutions are found near flow trajectories on the boundary between laminar and turbulent flow. In a long pipe, the attracting state on the laminar–turbulent boundary is a localized structure which resembles a smoothened puff. This 'edge' state remains localized even for Reynolds numbers at which the turbulent state is global.

1. Introduction

Laminar flow through a pipe is possible under controlled laboratory conditions up to flow rates well beyond those at which turbulence is typically observed. Pfenniger (1961) achieved laminar flow at Reynolds numbers as high as 100 000, $Re := UD/\nu$, where U is the mean axial speed, D the diameter and ν the kinematic viscosity, indicating that rather than the transition to turbulence being via a linear instability, some other mechanism must be responsible. Given an initial disturbance of sufficiently large amplitude, self-sustained turbulence is observed for Re of approximately 2000. This turbulent flow exhibits distinct spatial structures at different flow rates. For Re up to around 2250 the region of turbulence remains localized, with a length of approximately $20D$, and is referred to as a 'puff' (Wygnanski & Champagne 1973). At larger flow rates these puffs slowly delocalize by splitting into two or more puffs. At much larger Re, of around 2800, the disturbances develop into a rapidly expanding active region of turbulence, referred to as a 'slug'. No explanation has been offered that predicts such a progression in flow regimes, and many issues remain unresolved.

[1]Present address: Laboratoire d'Hydrodynamique, Ecole Polytechnique, 91128 Palaiseau, France
† Email address for correspondence: willis@ladhyx.polytechnique.fr

The dynamics of perturbations at transitional Reynolds numbers is believed to be strongly influenced by a rapidly increasing number of branches of exact solutions that have been found to appear at these Re (Faisst & Eckhardt 2003; Wedin & Kerswell 2004; Kerswell 2005; Pringle & Kerswell 2007; Pringle, Duguet & Kerswell 2008). At $Re < 1750$, puffs are observed to suddenly and unexpectedly decay in experiments (Peixinho & Mullin 2006), and it has been suggested that the turbulent state wanders between these unstable solutions before relaminarizing (Faisst & Eckhardt 2004; Hof *et al.* 2004). The same data also suggest that the mean lifetime for a puff becomes infinite at $Re = 1750$, indicating that the puffs become permanent states at this point (Peixinho & Mullin 2006). This critical Re has been reproduced to within 7 %, using numerical computations which adopted the experimental protocol for initiating the puffs and worked within a long periodic pipe of $50D$, so as to realistically capture the puff structure (Willis & Kerswell 2007*a*). However, experiments using a different way of initiating the puffs and designed to capture longer puff transients claim that no such critical Re exists (Hof *et al.* 2006). Simulations also presented there in a short $\approx 5D$ pipe appear to support this conclusion. The obvious question is then whether numerically simulated turbulence which fills a short pipe has the same relaminarization characteristics as localized puff turbulence captured in longer numerical domains. A complete statistical study using fully resolved three-dimensional computations across a spectrum of periodic pipe domains remains prohibitively expensive, whereas a survey using a realistic model system could provide a clarifying demonstration of difference.

Evidence has also emerged recently that many of the exact solutions known thus far sit on a separatrix between laminar and turbulent states, forming an 'edge' to the chaotic region of phase space (Kerswell & Tutty 2007; Schneider, Eckhardt & Yorke 2007*b*; Duguet, Willis & Kerswell 2008; Willis & Kerswell 2008). (See Itano & Toh 2001, Viswanath 2007 and Wang, Waleffe & Gibson 2007 for similar observations in channel and plane Couette flow.) Schneider *et al.* (2007*b*) have examined the dynamics of flow restricted to lie in this separatrix in a short $5D$ pipe, finding at long times a chaotic attractor apparently centred on a simple travelling wave solution (Pringle & Kerswell 2007). In such a short pipe, the turbulence naturally fills the pipe when triggered, and the laminar–turbulent boundary end state, or 'edge' state, is also a global state. In a longer ($\geqslant 25D$) pipe, however, localized puffs are the naturally triggered state at low Re, which raises the issue of what the corresponding 'edge' state is and how it varies with Re. For example is it initially localized, and does it lose localization at the same Re as the turbulent puff? Again, a realistic model system can suggest probable answers to these questions quickly.

The use of model systems is well established in plane Couette flow, which exhibits the same abrupt subcritical transition behaviour as pipe flow. Several approaches have been designed to reduce the number of degrees of freedom of this problem in order develop more tractable models. The minimal flow unit introduced by Jiménez & Moin (1991) has been useful in identifying the key components that lead to self-sustaining turbulence in a very small domain (Hamilton, Kim & Waleffe 1995). The model by Lagha & Manneville (2007) severely truncates the degrees of freedom in the cross-stream direction but captures spanwise and streamwise spatial structures observed in plane Couette flow. Using this model, attempts have been made to measure the lifetime of localized turbulence and determine the characteristic structures seen during the relaminarization process itself. Currently, such calculations would be prohibitively expensive for fully three-dimensional models. Severe truncation to only a few Fourier modes in the tilted crosswise direction has also proven useful in determining the origin of oblique bands in plane Couette flow (Barkley & Tuckerman 2007).

The aim of this paper is to establish a model system which preserves the rich dynamics of pipe flow but reduces the number of degrees of freedom of the system so considerably that the two current issues mentioned above can be probed. The price paid for this reduction is, of course, a close quantitative match with fully three-dimensional pipe flow. But this is more than counterbalanced by the ability to isolate and explore, for example, a 'puff-like' structure in a much more accessible system. The issues to be addressed *within* the reduced system are as follows: (*a*) Do the relaminarization statistics for turbulent puffs differ in character between short and long pipes? In particular, do long-pipe simulations indicate a critical Re for sustained puffs, whereas short-pipe simulations do not? (*b*) And what does the attracting 'edge' state in the laminar–turbulent boundary look like in a long pipe? Is it localized like a puff, and if so, does it delocalize at the same Re as a puff?

Previous attempts to find such a reduced model have focused on axisymmetric pipe flow (Patera & Orszag 1981) and helical pipe flow (Landman 1990*a*,*b*), but in both cases the subcritical dynamics of pipe flow is not retained. We briefly revisit these calculations to search afresh for evidence of turbulent transients before introducing a new $2+\epsilon$-dimensional model which retains the salient features of fully three-dimensional pipe flow. The presentation starts by discussing the formulation used for the calculations performed throughout this and earlier work (Willis & Kerswell 2007*a*, 2008).

2. Formulation

Given diameter D and fixed mean axial speed U, it is numerically convenient to scale lengths by $D/2$ and velocities by $2U$ in the Navier–Stokes equations, leading to

$$(\partial_t + \boldsymbol{u}\cdot\nabla)\boldsymbol{u} = -\nabla p + \frac{4}{Re}(1+\beta)\,\hat{\boldsymbol{z}} + \frac{1}{Re}\nabla^2\boldsymbol{u}, \tag{2.1}$$

where the non-dimensional variable β is the fractional pressure gradient, additional to the laminar flow, required to maintain a steady U. A Reynolds number Re_p, based on the applied pressure gradient, is given by $Re_p = Re\,(1+\beta)$. Our numerical formulation is based on the potential formulation of Marqués (1990), which is further re-expressed to ease numerical solution. An averaging operator is introduced in the axial direction, z, which is periodic over a length $L = 2\pi/\alpha$,

$$P_z(\cdot) = \frac{1}{L}\int_0^L (\cdot)\,\mathrm{d}z. \tag{2.2}$$

The velocity, $\boldsymbol{u}$, is then expressed in terms of a potential $\psi = \psi(r,\theta,z)$, the axially independent flow $h = h(r,\theta)$ and a purely axially dependent potential $\phi = \phi(r,\theta,z)$,

$$\boldsymbol{u} = h\,\hat{\boldsymbol{z}} + \nabla\wedge(\hat{\boldsymbol{z}}\psi) + \nabla\wedge\nabla\wedge(\hat{\boldsymbol{z}}\phi), \tag{2.3}$$

such that $P_z\phi = 0$. Writing the nonlinear terms as $\boldsymbol{b} = (\boldsymbol{u}\cdot\nabla)\boldsymbol{u}$, the governing equations become

$$\begin{aligned}
\left(\partial_t - \frac{1}{Re}\nabla^2\right) h &= -P_z\,\hat{\boldsymbol{z}}\cdot\boldsymbol{b},\\
\left(\partial_t - \frac{1}{Re}\nabla^2\right)\nabla^2\nabla_h^2\phi &= -(1-P_z)\,\hat{\boldsymbol{z}}\cdot\nabla\wedge\nabla\wedge\boldsymbol{b},\\
\left(\partial_t - \frac{1}{Re}\nabla^2\right)\nabla_h^2\psi &= \hat{\boldsymbol{z}}\cdot\nabla\wedge\boldsymbol{b},
\end{aligned} \tag{2.4}$$

where $\nabla_h^2 := \nabla^2 - \partial_{zz}$. For a boundary condition $\boldsymbol{u} = \boldsymbol{g}(\theta, z)$, conditions on the potentials are

$$h = 0, \quad \phi = 0, \quad -\partial_r \psi = g_\theta, \quad -\nabla_h^2 \phi = g_z, \tag{2.5}$$
$$\tfrac{1}{r}\,\partial_\theta \psi + \partial_{rz}\phi = g_r, \quad \partial_{rz}\nabla_h^2 \psi - \tfrac{1}{r}\partial_\theta \nabla^2 \nabla_h^2 \phi = Re\, \hat{\boldsymbol{r}} \cdot \nabla \wedge \boldsymbol{b} - \partial_{zz}\, \hat{\boldsymbol{r}} \cdot \nabla \wedge \boldsymbol{g}$$

(see Appendix A for details). Note that $\hat{\boldsymbol{r}} \cdot \nabla \wedge \boldsymbol{b} = 0$ on the boundary unless an internal body force is added. Variables are expanded in Fourier modes:

$$A(r, \theta, z) = \sum_{k,m} A_{km}(r)\, \exp(\mathrm{i}\alpha k z + \mathrm{i} m \theta). \tag{2.6}$$

As the variables are real, their coefficients satisfy the property $A_{km} = A^*_{-k,-m}$, where * indicates the complex conjugate, and therefore only the coefficients with $m \geqslant 0$ are kept. Numerical truncation in k and m is discussed in following sections. The operator P_z picks out $k = 0$ modes, and $(1 - P_z)$ retrieves $k \neq 0$ modes. In addition to the boundary conditions (2.5), regularity at the axis imposes symmetries on the Fourier modes across the axis. For the potentials, each mode is even or odd in r if m is even or odd, respectively.

The system for h is simple to solve, as it is second order and has two conditions on h, one at the boundary and a symmetry condition at the axis. The system for ψ and ϕ is more difficult to invert, as it is coupled through the boundary condition. To enable numerical solution we reformulate the system for ψ and ϕ into a set of five equations, each second order in r, and use an influence matrix technique to bypass the coupled boundary condition (see Appendix B for details).

Both finite-difference and Chebyshev expansions have been used in radius. The latter is better at low radial resolution, but the former involves only banded matrices (a 9-point stencil is used), requiring less memory, and is faster for high radial resolutions. Time discretization is second order, using Crank–Nicolson for the diffusion term and a Euler predictor step for the nonlinear terms. Information from a Crank–Nicolson corrector step is used to control the time step size. Nonlinear terms, $\boldsymbol{b}$, are evaluated using the pseudo-spectral method and are dealiased using the 3/2 rule. The code was tested to reproduce eigenvalues about the laminar state, eigenvalues about nonlinear travelling wave solutions from Wedin & Kerswell (2004), by direct comparison with a primitive variable code (Kerswell & Tutty 2007) during the relaminarization of a perturbed travelling wave, and to calculate the turbulent statistics of Eggels *et al.* (1994).

3. The absence of turbulence in previous models

The original calculations for axisymmetric pipe flow (Patera & Orszag 1981) and helical flow (Landman 1990*a*) found no evidence for turbulence or even long transients at $Re \leqslant 4000$. Here we show that this conclusion extends to Re as large as 10^5 and huge initial disturbances, suggesting that there are no exact unstable solutions beyond Hagen–Poiseuille flow within these dynamical subspaces.

The axisymmetric model is straightforward to simulate using the numerical algorithm described above by time stepping only the modes with $m = 0$. In helical flow, variations in θ and z are reduced to a dependency in the one variable $\xi = \theta + \alpha z$, where α is the pitch of the helix, and periodicity over $L = 2\pi/\alpha$ is preserved. In this scenario the flow may be expanded, $\boldsymbol{u}(r, \xi) = \sum_q \boldsymbol{u}_q(r) \exp(\mathrm{i}q\xi)$, corresponding to taking only modes $k = m \to q$ in our formulation. Letting $\boldsymbol{u}'$ be the deviation from

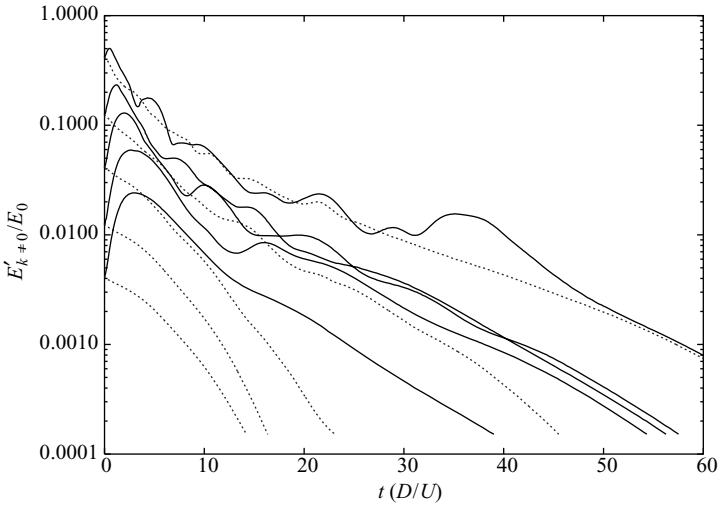

FIGURE 1. Decay of axisymmetric (dashed) and helical (solid) perturbations, initially of energy up to 40 % of the laminar profile ($Re = 10\,000$ and pipe $2\pi D$ long).

the laminar flow, random initial disturbances of the form

$$\boldsymbol{u}' = \sum_{k^2+m^2\neq 0} r^2(1-r)^2\,(\alpha^2k^2+m^2)^{-\frac{1}{2}}\,\boldsymbol{a}_{km}\exp(\mathrm{i}\alpha kz+\mathrm{i}m\theta), \tag{3.1}$$

were applied to the flow (after projection onto the space of solenoidal functions to enforce incompressibility), where the components of $\boldsymbol{a}_{km}$ were random numbers in $\mathbb{C}$ s.t. $|a_{km}| = 1$.

Figure 1 shows time evolution of random disturbances at $Re = 10\,000$ for a pipe of length $2\pi D$. Initial disturbances were normalized for $E'_{k\neq0}/E_0$ up to 0.4, where $E'_{k\neq0}$ is the energy of the axially dependent modes and E_0 is the energy of the laminar profile; i.e. disturbances of up to 40 % of the energy of the laminar flow were considered. By way of comparison, the turbulent test case of Eggels *et al.* (1994) has only $E'_{k\neq0}/E_0 \approx 0.014$ at $Re = 5300$. The number of finite difference points in radius and truncation of the Fourier modes was (160, $\pm$256) in (r, z) and (r, ξ); the large radial resolution was required to stably solve for such high initial energies. Axisymmetric disturbances show little sign of nonlinear interactions at this Re and decay almost monotonically. Five other sets of runs for other random disturbances showed similar behaviour. Helical flow is slightly more promising, showing occasional moments of growth against a dominant decay.

Helical flow exhibits a linear instability at relatively small rotation rates about the axis, which occurs at longer L for larger Re (Mackrodt 1976). This supercritical bifurcation and the subsequent nonlinear waves (Toplosky & Akylas 1988; Landman 1990*b*) provided an excellent test of the helical code. Measuring the rotation rate by $R_\Omega = (1/4)\Omega\,Re$, where the angular velocity Ω is in units U/D, there is a supercritical bifurcation to helical waves at $R_\Omega = -52.43$, $Re = 4000$ and $L = 16\pi D$. Figure 2 shows evolution of five random initial disturbances of $E'_{k\neq0}/E_0$ up to 0.3 in the presence of rotation – truncation at (80, $\pm$128) in (r, ξ). For $R_\Omega = -50$ the flow quickly returns the the parabolic profile. At $R_\Omega = -100$ and -300, well beyond the linear instability, the flow rapidly returns to a finite-amplitude helical wave flow. This supercritical behaviour persists for modest rotations so that no long-term turbulent

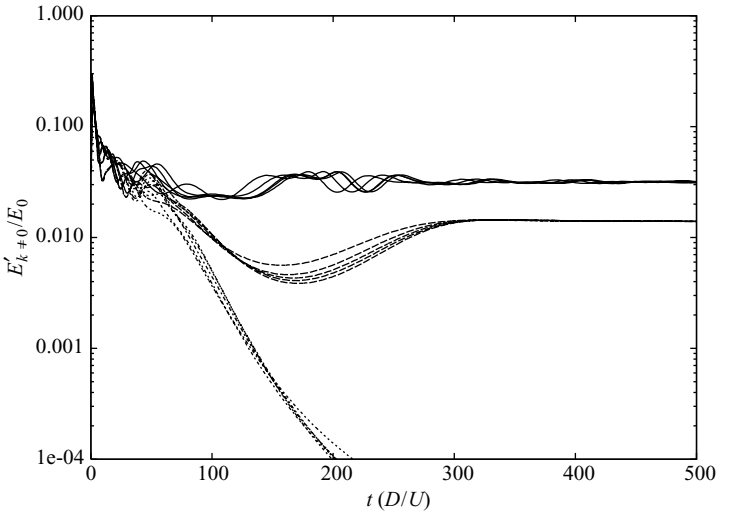

FIGURE 2. Large helical disturbances scaled from 4 % to 20 % of E_0 rapidly settle to parabolic flow for $R_\Omega = -50$ and to laminar helical waves for $R_\Omega = -100, -300$ ($Re = 4000$, $L = 16\pi D$).

transients can be generated. Barnes & Kerswell (2000) have shown that these helical waves themselves undergo a supercritical Hopf bifurcation so that solutions cannot obviously be traced back to non-rotating flow. Figure 2 suggests that disconnected branches which could lead to subcritical turbulence in rotating helical pipe flow are unlikely to exist.

Our calculations suggest that rotating helical pipe flow follows the supercritical route to turbulence via a sequence of supercritical bifurcations rather than the abrupt subcritical behaviour of three-dimensional non-rotating pipe flow. Having seen strong decay at Re approximately five times that for which turbulence is observed in the laboratory, it appears that neither dynamics restricted to helical nor axisymmetric subspaces are relevant for the observed transition.

4. A $2+\epsilon$-dimensional model

We now introduce a third model which has high resolution in the cross-stream (radial) and streamwise (axial) directions but only a few modes in the spanwise (azimuth) direction. The model was chosen to preserve a high radial resolution, as streak features close to the wall appear to be important in the self-sustaining process as do detachments from the wall during the relaminarization stages of low Reynolds number turbulence. High axial resolution was retained to allow the possibility of localized turbulent structures. This left only the azimuthal direction in which to reduce the number of degrees of freedom: only Fourier modes $m = 0, \pm m_0$ were considered, which corresponds to a sinusoidal variation in azimuth, an azimuthal shift of the sinusoid and a mean mode.

4.1. *Spatial characteristics*

Localized structures, surprisingly similar to puffs, were captured by the $2+\epsilon$-dimensional model. Figure 3 compares a puff structure from a simulation fully resolved in azimuth (all m up to ± 24) with a 'puff' from the $2+\epsilon$-dimensional model ($m = -3, 0, 3$). The plots are of the correct aspect ratio, but only half of the computational domain is shown. Puffs from the model appear to be similar to

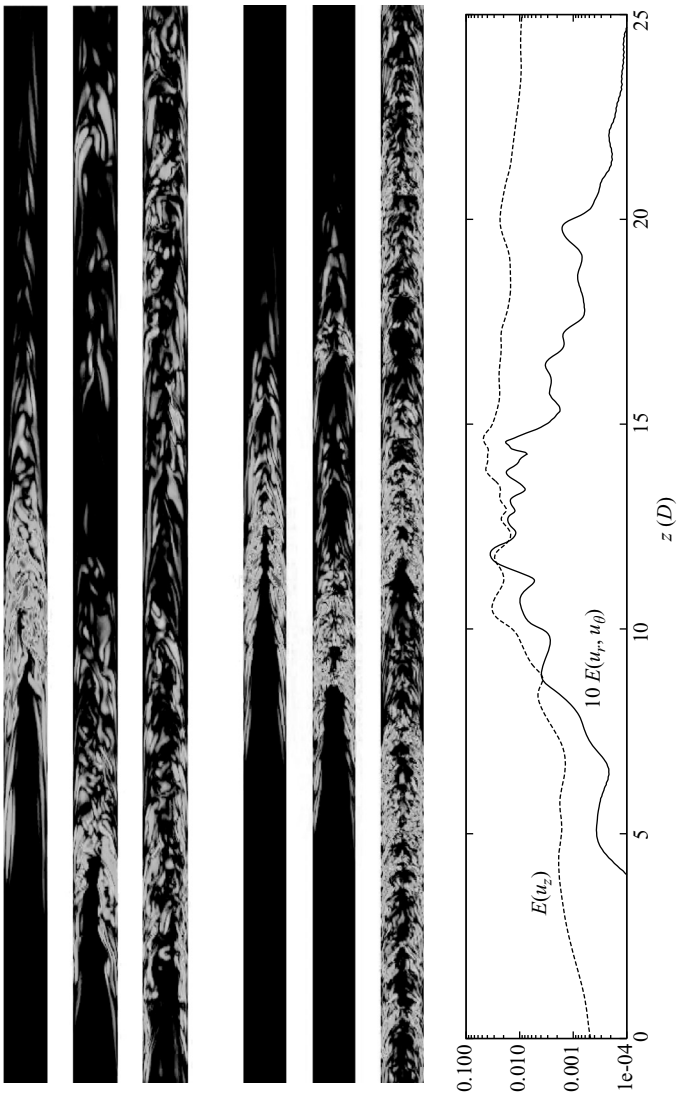

FIGURE 3. Axial vorticity in the (r, z)-plane, 1:1 aspect ratio, flow up the page; only $25D$ of a periodic $50D$ domain shown. *From left to right*: fully three-dimensional simulations at $Re = 2000$, 2300, 2700 and $2+\epsilon$-dimensional simulations at $Re = 2600$, 3200, 4000. Presented for both models are localized 'puffs', the early stages of delocalization by the generation of a second puff downstream and global slug turbulence at larger Re. *Far right*: Energy in separate components of the velocity as a function of axial position (units D^2U^2) for the model puff snapshot at $Re = 2600$.

resolved puffs in both length and structure, having a smooth upstream region close to the wall, an active turbulent region and a dissipative region downstream (although note the different Re). Only modest radial resolutions were required to observe such structures: a spectral resolution of 35 Chebyshev modes was used for the calculations of this section. Several calculations were performed with a lower resolution of 25 radial modes, but puff structures tended to elongate, requiring a longer pipe and thus offsetting the reduction in computation times. The energy plot in figure 3 shows that the while the axial deviation from the mean flow is extended, $20\,D$ or greater, the

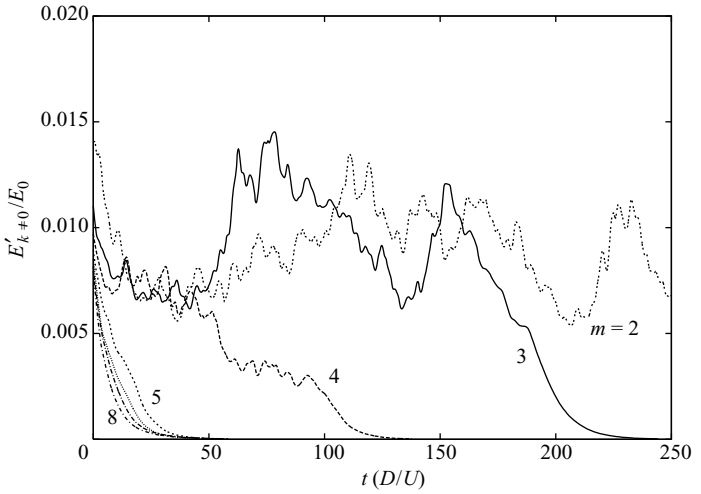

FIGURE 4. Initial trials of the $2+\epsilon$-dimensional model for several m-fold rotational symmetries.

roll components are highly localized, extending only 5–10D. Such localization of the active region of the flow has been observed in the fully three-dimensional case (Willis & Kerswell 2008).

Axial resolution was chosen to approximately match the spectral drop-off in r (approximately four orders in the magnitude of the spectral coefficients or eight orders in the power spectrum) and was ± 384 for $L = 16\pi D \approx 50$ diameters. Axial resolution was changed proportionally for other L considered in the rest of this section, hence keeping the smallest resolved scale fixed. Puffs were found to translate within 2 % of U, slightly faster than in three dimensions, where they travel approximately 10 % slower. Also shown in figure 3 is that the transition from localized to global turbulence is gradual, as observed experimentally. At larger Re the puff becomes delocalized, splitting into two or more localized turbulent regions with relatively laminar regions in between. At much larger Re the proportion of vigorous turbulence is seen to increase, as recorded by Gilbrech & Hale (1965).

4.2. *Temporal characteristics*

Another important feature captured by the model is that localized puffs may survive for long times before a sudden decay as observed experimentally (Peixinho & Mullin 2006). Typical transients for different m_0 are shown in figure 4 which indicates that higher rotational symmetries tend to decay more quickly. As structures of threefold rotational symmetry are the most frequently observed for transitional Re (Duggleby *et al.* 2007; Kerswell & Tutty 2007; Schneider, Eckhardt & Vollmer 2007*a*; Willis & Kerswell 2008), $m_0 = 3$ was chosen for analysis of the lifetimes of disturbances. For this m_0, azimuthal length scales are also comparable to the radial length scale in the model. Figure 5 shows the probability distribution function for puff lifetimes based upon 100 runs at each of several Re in a pipe $\approx 100D$ long ($L = 32\pi D$). Sets of initial puff conditions were generated from snapshots of a long run at a sufficiently large Re, similar to the annealing procedure adopted in Peixinho & Mullin (2006) and Willis & Kerswell (2007*a*). No dependence on the initial condition was observed, however, other than in the very early times of the transient. For the model, times of order $10^4\, D/U$ could be achieved, significantly longer than achieved in Willis & Kerswell

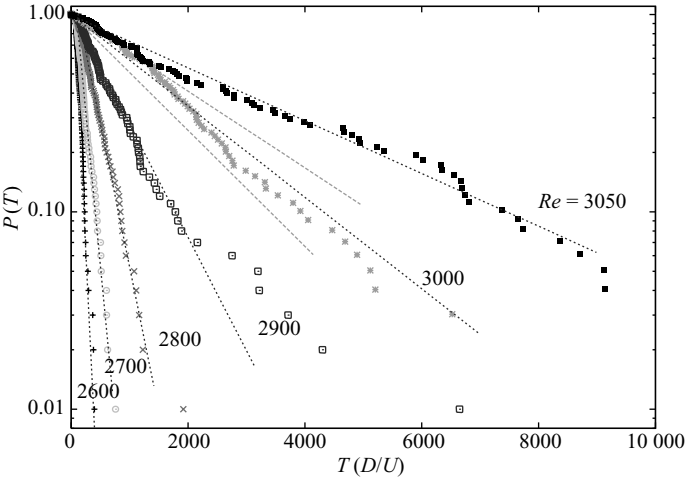

FIGURE 5. Probability of transient surviving to time T in the $m_0 = 3$ model for a pipe of ≈ 100 diameters ($L = 32\pi D$); 100 observations per Re. See the text for how the 'best fit' lines were drawn.

(2007*a*) and in less computation time. The log-plot shows an exponential distribution indicating a memoryless process.

Slopes in figure 5 are based on a median time τ calculated by the bootstrapping method adopted in Willis & Kerswell (2007*b*). The shorter slopes represent 95 % confidence intervals for the slope of the data at $Re = 3000$, and are accurately calculated by the bootstrapping method. The best fit line was found to be poor estimator of the mean, being overly sensitive to rare events (e.g. the outlier in figure 5 for $Re = 2900$), and the goodness-of-fit does not provide the correct error estimate. In the bootstrapping method, samples of size N are generated by resampling from the original N observations, with equal probability of selecting each. This is repeated 100 000 times, and the distribution of the means of the samples provides an accurate confidence interval for the mean of the original data set. When all data fall within a maximum observation time, the confidence intervals generated by this method converge to those predicted by the central limit theorem. A 95 % confidence interval for τ is approximately $\tau \pm 2\tau/\sqrt{N}$. The method is particularly useful when the data are truncated in time, and therefore a mean cannot be directly calculated. The bootstrapping method easily accommodates such data by further resampling when a truncated point is chosen. Any additional error associated with the extra resampling is reflected in a wider confidence interval.

Estimating the median lifetime of a puff from the data is subject to two sources of error: the initial transition period during which the flow evolves from the initial condition to become a puff and the presence of a final relaminarization phase. The former is eliminated by considering each of the first observations as an initial cutoff time and by examination of the effect of the cutoff on the estimator τ. See Willis & Kerswell (2007*b*) for an example plot of τ with confidence intervals versus number of observations cut. Removing the first few observations eliminates the effect of the transient on τ but slightly widens the confidence interval. The relaminarization time error was minimized by identifying a threshold three-dimensional energy below which the turbulent flow always relaminarizes and applying the same value to all runs to indicate the end of the puff lifetime ($E'_{k\neq 0}/E_0 = 0.001$).

	Global turbulence		Localized turbulence	
$L\,(D)$	a	b	β	Re_c
2π	-2.5×10^{-3}	6.2		
4π	-4.3×10^{-3}	11.6		
8π	-6.5×10^{-3}	18.1	5.9 ± 2.0	≈5000
16π			4.6 ± 1.6	3575
32π			4.8 ± 1.6	3450

TABLE 1. Best fit parameters for an exponential fit $1/\tau=\exp(aRe+b)$ and an algebraic fit $1/\tau=(Re_c-Re)^{\beta}$ for different lengths of periodic pipe.

The median time $\tau(D/U)$ is dependent on the parameter Re. As mentioned above, whether τ diverges to infinity or not at a finite Re is a matter of ongoing debate. In laboratory experiments using a pipe with $D=20\,\mathrm{mm}$, $L=785D$, Peixinho & Mullin (2006) found evidence that $\tau\sim1/(Re_c-Re)$ with $Re_c=1750$. In contrast, experiments by Hof *et al.* (2006) for $D=4\,\mathrm{mm}$, $L=7500D$, using a different method to initiate the puff, found that $\tau\sim\exp(c_1Re)$, for some constant c_1. Numerical experiments by Willis & Kerswell (2007*a*,*b*) using well-resolved puffs in a $50D$ periodic pipe, however, show lifetimes to be significantly different from the exponential scaling, and the simple power -1 was clearly seen with $Re_c=1870$, overestimating the experimental value of 1750 (Peixinho & Mullin 2006) by only 7 %. Computational and experimental limitations have confined observations of τ to $O(10^3-10^4)\,D/U$.

Figure 6 shows the maximum likelihood estimator for $1/\tau$ and 95 % confidence intervals across a spectrum of pipe lengths. Lifetimes an order of magnitude larger than the calculations of Willis & Kerswell (2007*a*) were possible in a pipe twice as long, $L\approx100$ diameters. In short pipes (figure 6*a*), where turbulence fills the domain and is therefore global, the lifetime appears to follow an exponential scaling $1/\tau=\exp(aRe+b)$ with values for a and b given in table 1. The $8\pi D$ (≈25 diameter) pipe represents a crossover situation in that the turbulence is only truly pipe-filling for the highest two data points, whereas it is localized for the four lower Re shown in figure 6(*a*). An exponential fit through just the two higher Re points, however, seems to fit a steepening trend as the pipe lengthens, suggested by the $2\pi D$ and $4\pi D$ data sets.

The remaining localized-turbulence points for $L=8\pi D$ are better fit by an algebraic expression $\tau=1/(Re_c-Re)^{\beta}$ (see table 1 for Re_c and β). The fit includes two extra points at lower Re for the $8\pi D$ pipe shown in figure 6(*b*). Doubling to a $16\pi D$ (≈50 diameter) pipe produces a rapid drop in $1/\tau$ and a more clearly defined curvature in the data. This length increase is significant because the turbulent 'puffs' in this reduced model are approximately $20D$ long (see figure 3). Hence, while such puffs will be significantly affected by enforced periodicity over ≈25 diameters, this artificial constraint should be substantially relaxed in an ≈50 diameter pipe and almost absent in a pipe of ≈100 diameters. By way of confirmation, a $32\pi D$ pipe produces relaminarization data very similar to that of the $16\pi D$ pipe with both being fitted well by the relation $\tau\sim1/(Re_c-Re)^{\beta}$ based upon similar values for the fitting parameters (see table 1). Even though the exponent β is relatively poorly constrained, it is clearly different from the value of one which is observed in fully three-dimensional simulations (Willis & Kerswell 2007*a*) and experiments (Peixinho & Mullin 2006). This quantitative discrepancy is undoubtedly an artefact of the reduced

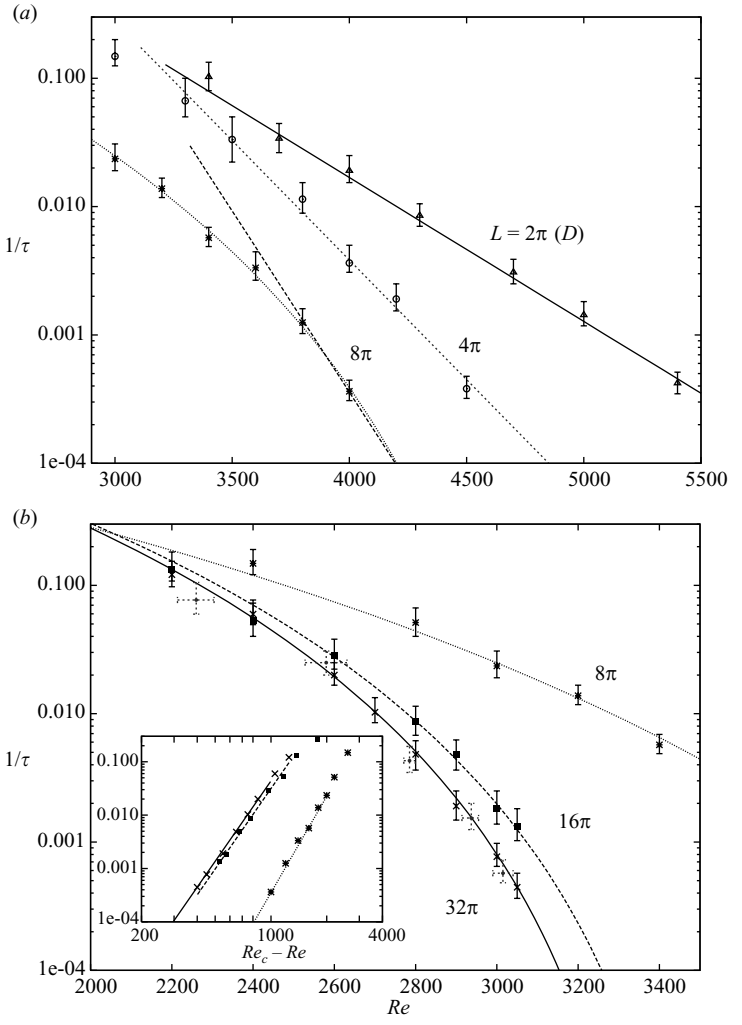

FIGURE 6. Sensitivity of the lifetime, $\tau(D/U)$, of transients to the pipe length. (*a*) The data for pipe lengths 2π, 4π and 8π (in D) and exponential fits, $1/\tau = \exp(aRe + b)$, through all points which correspond to global (slug) turbulence. The four leftmost data points for 8π correspond to localized (puff) turbulence, and a $1/\tau \sim (Re_c - Re)^{\beta}$ fit is shown for these. (*b*) The data for which localized (puff) turbulence is present for pipe lengths 8π, 16π and $32\pi \approx 100$ diameters long. Here the best fit lines take the form $1/\tau \sim (Re_c - Re)^{\beta}$, where the $1/\tau$ versus $(Re_c - Re)$ plot on log–log scales (inset) shows these fits as straight lines. (The same best fit line for $L = 8\pi D$ is plotted in both *a* and *b*.) Points with error bars in Re were calculated using a fixed pressure gradient as opposed to fixed mass flux. This data is plotted using the time-averaged Re for a $32\pi D$ pipe and falls precisely on the fixed mass-flux data. (As for all other points, 100 observations were used for each.)

model and, in fact, is typical of other models for different flows (Bottin & Chate 1998; Lagha & Manneville 2007). What this reduced model does clearly exhibit, however, is a *qualitative* change in relaminarization behaviour when the preferred localized turbulent state (a 'puff') is allowed to develop. If the pipe is long enough to accommodate a 'puff', the presence of a critical Re is suggested, whereas when the pipe is shorter than a 'puff' so that the turbulence is always global, no such

critical threshold is suggested. This behavioural change is entirely consistent with the seemingly contradictory results obtained recently, using fully three-dimensional Navier–Stokes calculations in short $5D$ pipes (Hof *et al.* 2006) and long $50D$ pipes (Willis & Kerswell 2007*a*).

4.2.1. *Constant pressure gradient versus constant mass flux*

The reduced model was also used to investigate another open issue: is the form of driving, being either a constant, imposed pressure difference between the ends of the pipe or a constant, imposed mass flux, important for the relaminarization behaviour of turbulent puffs? Hof *et al.* (2006) use a pressure-drop set-up (constant mean pressure gradient) in their experiments over a very long pipe, whereas Peixinho & Mullin (2006) suck fluid through their pipe to produce a constant mass flux. In an averaged sense, the two methods of driving the flow are equivalent, but instantaneously and locally the flow dynamics are different – the mass flux rate can fluctuate for a constant mean pressure gradient flow, and local variations in the pressure gradient cause fluctuations in the total pressure drop for a constant flux flow. Hence puffs evolving in the two situations are subtly different, and it is therefore a leading question as to whether they possess the same relaminarization behaviour.

To answer this, a series of constant pressure-gradient runs were performed in the $32\pi D$ pipe, using randomly selected initial conditions from the same long puff run as for the constant mass flux runs. Again 100 runs were calculated for each data point at a given pressure gradient and then the median lifetime plotted as a function of Re in figure 6(*b*). Note that a horizontal error bar is plotted which indicates $\pm$ standard deviation in the mean Re value. At the largest mean pressure gradient used, the mean flow rate was $Re = 3050$ with fluctuations having one standard deviation of ± 25. This error in Re should inversely scale with the length of pipe for flow driven by a pressure head, provided that the disturbance remains localized. For the long pipe of Hof *et al.* (2006) such variations should be insignificant (1 part in 10^4), whereas for a short (numerical) periodic pipe very large variations $O(10\,\%)$ can be expected. The new data points sit precisely on the $32\pi D$ constant mass-flux curve, indicating that for at least the long pipe ($\approx$100 diameters), the precise form of driving is unimportant for the probability of puff relaminarization.

4.3. *Characteristics of the laminar–turbulent boundary: short pipe*

Given an initially laminar flow, small perturbations decay back to the laminar flow, and larger perturbations develop into turbulence for sufficiently large Re. This naturally leads to the question of what characterizes the dividing set of flows, for which a small perturbation may lead to either laminar or turbulent flow. Itano & Toh (2001) used a shooting method to find such a boundary in channel flow and discovered that the flow trajectory on the boundary settled upon what they thought was a travelling wave solution but which was later identified as a slowly varying part of a periodic orbit (Toh & Itano 2003). This orbit is stable within the manifold of flows on this laminar turbulent boundary or 'edge'. A similar situation is found in plane Couette flow (Viswanath 2007; Schneider *et al.* 2008), where a single simple attractor is found. Pipe flow exhibits different characteristics, however, with Schneider *et al.* (2007*b*) finding a chaotic attractor in which trajectories pass near exact travelling wave solutions (Mellibovsky & Meseguer 2007; Duguet *et al.* 2008). When the laminar–turbulent boundary dynamics are restricted within certain symmetry subspaces, however, simple attractors do emerge (Duguet *et al.* 2008).

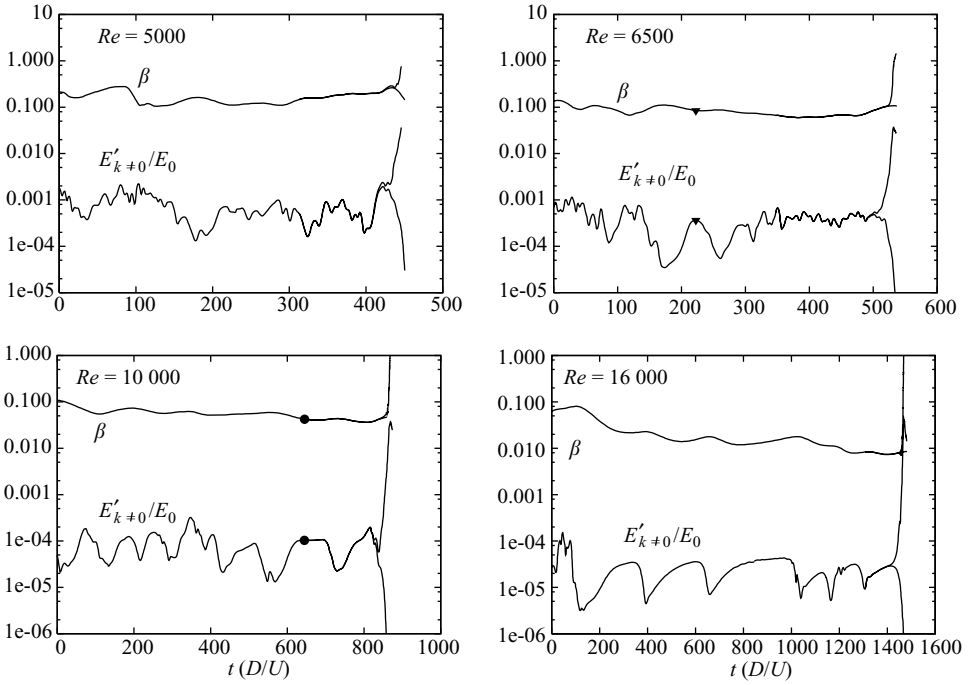

FIGURE 7. Edge trajectories for $L = \pi D$. Exact travelling wave solution found near the triangle at $Re = 6500$ (shown in figure 8) has very similar structure to that found at the circle for $Re = 10\,000$.

Pipe flow is not so different from channel flow, and yet they display different dynamics on the boundary. It is not difficult to imagine therefore that the severe truncation of our model could also lead to a loss of chaotic behaviour on the boundary. In this section we show that the model preserves the chaotic end state for trajectories on the boundary and that exact solutions exist. This motivates extension of the results to long computational domains, where undirected three-dimensional calculations would be prohibitively expensive.

Boundary or edge trajectories for the model are shown in figure 7, for $L = \pi D$ and over a range of Re. While a difference between the edge and developed turbulence may be seen by a rapid increase in energy, a clearer measure appears to be β related to the pressure gradient required to maintain the fixed flux (see (2.1)) or equivalently the friction. The pressure gradient is less than 10 % greater than the laminar value when on the edge and is also smooth in time, whereas after a sudden increase to turbulence it varies as rapidly as the energy. At the lowest Re shown in figure 7 the energy of the edge is highly variable in time. At the next $Re = 6500$ a period of slow variation is observed. Duguet *et al.* (2008) have recently demonstrated that the edge can be used to find exact solutions by identifying phases in which the flow has a relatively simple temporal behaviour. Such an episode is marked by a triangle, where the instantaneous flow is used as an initial condition for a Newton–Krylov code. This converges to the exact solution pictured in figure 8(*a*), confirming that travelling wave solutions do exist for the model. The flow exhibits fast streaks towards the walls, and slow streaks are shed towards the centre. The state found is also very similar to that marked by a circle at $Re = 10\,000$, when the trajectory for a while appears to settle towards a steady (translating) state. As Re increases the variability on the

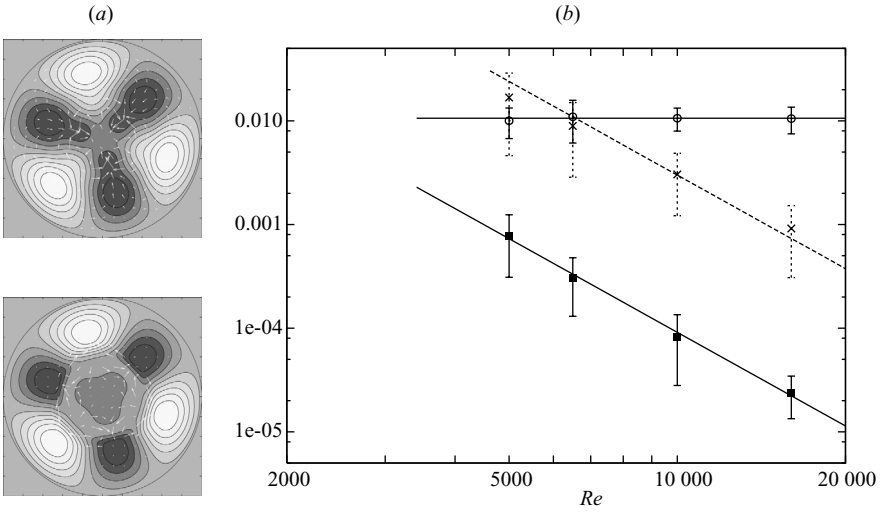

FIGURE 8. (*a*) Cross-sections of an exact travelling-wave solution $L = \pi D$, $Re = 6500$, wave speed $c = 1.563\,U$ at $z = 0, (1/2)L$. Dark regions are slower than the laminar profile and white regions faster. (*b*) Normalized energy $E'_{k\neq 0}/E_0$ on the boundary (squares) and of turbulence (circles). The crosses indicate the normalized total disturbance energy E'/E_0 on the boundary. The slope for the total disturbance energy (and also $E'_{k\neq 0}/E_0$) is -3, implying that the disturbance amplitude $A \sim Re^{-1.5}$. At $Re = 5300$, $E'_{k\neq 0}/E_0 \approx 0.011$ in the reduced model and ≈ 0.014 in the fully three-dimensional test case.

edge surprisingly decreases, more so than can be explained by the increasing viscous time. The viscous time D^2/ν scales as Re in our time units, and longer trajectories at larger Re have been shown in figure 7 to compensate. A possible explanation for the decreasing variability is that the eigenvalues of the unstable directions from the travelling waves decrease with increasing Re as in plane Couette flow (Viswanath 2007; Wang *et al.* 2007), thus enabling closer and longer visitations.

The variability of the boundary in terms of energy or any other chosen amplitude measure also, of course, indicates the range of such attributes for initial conditions which will trigger turbulence. The fact that it is easier to trigger turbulence as Re increases (e.g. Hof, Juel & Mullin 2003) is reflected in the decrease in the mean boundary energy as Re increases seen in figure 8(*b*). Error bars in this figure represent the mean and one standard deviation above and below this mean, but nevertheless, a clean scaling emerges for the disturbance amplitude of $A \sim Re^{-1.5}$. Mellibovsky & Meseguer (2006) found this scaling when considering streamwise perturbations and Peixinho & Mullin (2007) in laboratory experiments with obliquely oriented jets.

4.4. *Characteristics of the laminar–turbulent boundary: long pipe*

The bisection procedure (Itano & Toh 2001; Schneider *et al.* 2007*b*; Duguet *et al.* 2008) for isolating the laminar–turbulent boundary can equally be applied to flow within a long pipe, although the computational demands become increasingly intensive. The $2+\epsilon$-dimensional model is ideal for a reconnaissance of likely behaviour, including identification of the form the edge state takes. With this motivation, trajectories on the laminar–turbulent boundary were found for a pipe ≈ 50 diameters long, using the pressure gradient to distinguish between edge and turbulent flow states. Interestingly, the attracting edge state which emerges looks exactly like a turbulent puff except at the trailing edge (upstream region): compare figures 3 and 9(*a*). In a turbulent puff

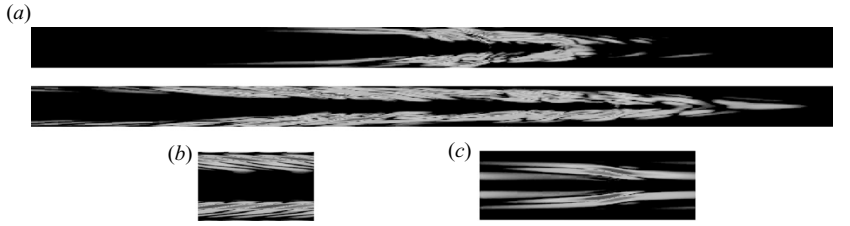

FIGURE 9. (*a*) Snapshots of axial vorticity at two different times from a laminar–turbulent boundary trajectory; $L = 16\pi D$, $Re = 4000$; $20D$ of $\approx 50D$ shown. The disturbance is localized but with an extended upstream region. (*b*) An exact solution shown over two axial periods, $L = 1.694D$, discovered using the code of Pringle & Kerswell (2007). (*c*) The exact solution of figure 8 found by the Newton–Krylov code of Duguet *et al.* (2008), $L = \pi D$.

this is the most energetic part possessing a fluctuation energy level comparable to homogenized slug turbulence (see Willis & Kerswell 2008) at higher Re. However, the edge state is noticeably smoother even at $Re = 4000$ (figure 9) compared to a puff at $Re = 2600$ (figure 3) which has finer scales. The similarities between the two are the strong wall structures slanting into the axis at the upstream region, a region in which the axial vorticity reaches the axis (the trailing edge region), followed by a gradual relaminarization/decay downstream. Interestingly it is the upstream region that waxes and wanes (compare the two axial vorticity snapshots of figure 9) rather than the passive-looking downstream wake.

The edge state remains localized just like the turbulent puff up to $Re = 3000$, but surprisingly it also remains localized for much higher Re when the puff has given way to (global) slug turbulence. To emphasize this, the localized edge state shown in figure 9 at $Re = 4000$ was generated starting from the global disturbance of figure 3. The fact that the edge state remains puff-like throughout the puff-to-slug transitional Re range suggests that slug turbulence is destabilized puff turbulence rather than a separate state occupying a different part of phase space. This is certainly consistent with simulations in which a puff state smoothly evolves into a slug by slowly expanding upstream as well as downstream. A corollary of this, of course, is that a puff and a slug cannot coexist at a given Re: to our knowledge there are no reported experimental observations to contradict this claim.

Figure 9 also shows the axial vorticity for a travelling wave with shift-and-reflect symmetry, found using the method of Pringle & Kerswell (2007), and for the travelling wave shown in figure 8 (which has no special symmetry). Both have axial vorticity slanted from the wall into the central axis reminiscent of the turbulent puff and edge state. A recent search for coherent fast-streak states within turbulent puffs has indicated that the flow transiently resembles travelling wave states upstream and downstream of the trailing edge region (Willis & Kerswell 2008). Given that the energetic trailing edge region is absent in the edge state, there seems an even higher likelihood of seeing coherent states there.

Although the findings in this $2+\epsilon$-dimensional model are only suggestive of what may occur in the fully three-dimensional setting, they are sufficiently interesting to motivate a fully three-dimensional long-pipe computation. This is currently underway.

5. Discussion

In this paper, we have described the numerical formulation used to simulate transitional pipe flow (Willis & Kerswell 2007*a*, 2008; Duguet *et al.* 2008). This is based

upon the poloidal–toroidal potential decomposition of the velocity field discussed by Marqués (1990), where the difficulty of coupled boundary conditions has been bypassed by influence matrix methods here. Reducing the system to five simple second order equations, the method is accurate, relatively simple to implement and computationally efficient. This has then been used here to explore dynamic subspaces in the hope of finding a reduced system to aid understanding.

No evidence for turbulent transients has been found in axisymmetric pipe flow, confirming an earlier investigation (Patera & Orszag 1981), or in helical pipe flow, consistent with the work by Landman (1990*a*, *b*). Rotating pipe flow displays a classic supercritical bifurcation route to turbulence (Mackrodt 1976; Toplosky & Akylas 1988; Landman 1990*a*, *b*; Barnes & Kerswell 2000) which has no bearing on the non-rotating situation. A brief search in rotating helical pipe flow failed to find evidence for any disconnected subcritical branches of solution which may have reached back to the non-rotating limit. A $2+\epsilon$-dimensional model, which represents a minimal three-dimensionalization of the axisymmetric limit, does, however, possess a subcritical transition scenario and all the important spatio-temporal characteristics of fully resolved pipe flow at Re of the same order of magnitude. Localized disturbances, structurally similar to turbulent puffs, are found in the model at low Re ($\approx$2600), which slowly delocalize at intermediate Re ($\approx$3200) and rapidly expand into slugs at high Re ($\approx$4000). Exact unstable travelling wave solutions also exist within the model and appear to underpin the dynamics in phase space.

Within this $2+\epsilon$-dimensional model, the relaminarization statistics of the puffs have been examined in pipes of varying lengths. For pipes long enough to allow localized turbulence to manifest itself, a critical Re is suggested by the data above which the 'puff' becomes sustained. On the other hand, if the pipe is short so that turbulence fills the whole domain, the data are consistent with only transient behaviour; i.e. the turbulence always dies eventually. This qualitative change in behaviour as the computational domain is varied is consistent with the seemingly contradictory results found recently in fully three-dimensional simulations (Hof *et al.* 2006; Willis & Kerswell 2007*a*). The need to resolve the spatial inhomogeneity of the puff state properly in numerical experiments is clear.

Reconciling the conclusions drawn from the experimental data sets (Hof *et al.* 2006; Peixinho & Mullin 2006) remains a challenge. The existence of both types of $\tau - Re$ scalings are not mutually exclusive, however, and resolution of the issue may be related to the known sensitivity of the flow to the exact structure and amplitude of a perturbation. Experiments (Darbyshire & Mullin 1995) and simulations (Faisst & Eckhardt 2004; Moehlis, Faisst & Eckhardt 2004) have indicated that the laminar–turbulent boundary has a fractal-like structure in which very small changes to the perturbation can completely change the fate of the flow; finite lifetimes can then exist in the presence of an attractor because an initial disturbance, apparently large enough to trigger a puff, may actually not be within its basin of attraction (e.g. Moehlis *et al.* 2004; Mullin & Peixinho 2006). In addition, if the laminar–turbulent boundary is closely intertwined with the attractor in phase space, a trajectory can easily be nudged out of the attractor by noise effects, such as pipe roughness, temperature changes, pipe misalignment and vibrations. Noise-induced relaminarizations of established puffs for Re above Re_c do not therefore contradict the existence of a critical Re. Conversely, noise could also artificially maintain puff turbulence in the absence of an attractor. There is clearly a need for further experimentation.

It is worth remarking that longer transients in the $100D$ pipe (i.e. Re closer to Re_c) could, in principle, have been calculated given the computational savings available in

the model. It was found, however, that the puffs begin to delocalize for $Re \approx 3200$, indicating that by $Re_c = 3450$, the puff has become unstable to slug-like turbulence. The same issue occurs in the real system: puffs delocalize to become slugs for $Re = 2250$–2500 (Willis & Kerswell 2008). No claim has been made in the literature that expanding slugs are other than permanently sustained once generated.

The $2+\epsilon$-dimensional model has also presented an opportunity to probe the possible dynamics on the laminar–turbulent boundary in long-pipe flow. Calculations indicate that the attracting state in this set is a localized puff-like structure which is smoother and less energetic in the trailing edge region than its turbulent puff counterpart. Also intriguingly, this end state remains localized way beyond in Re when the puff has delocalized. This tends to suggest that the turbulent puff still exists as a solution but has become unstable to a slug state. The variability of the flow on the laminar–turbulent boundary also highlights the variability in initial conditions, which can trigger turbulence. Just focusing on the mean energy gives a disturbance amplitude scaling $A \sim Re^{-1.5}$ consistent with some numerical computations (Mellibovsky & Meseguer 2006) in a short pipe and laboratory experiments with a carefully specified jet configuration, designed to excite a coherent vortex (Peixinho & Mullin 2007). Clearly, exploring how far this realization can be usefully developed is a promising area for future research.

In conclusion, we have introduced a model of pipe flow severely truncated in its azimuthal degrees of freedom but otherwise fully resolved. This notwithstanding, the remaining system captures all of the rich dynamical behaviour observed in pipe flow but obtained at a fraction of the computational cost for the full three-dimensional situation. It therefore presents a very accessible arena in which to test ideas and gain some insight quickly before deciding to invest a considerable effort in the full three-dimensional system.

Many thanks to Yohann Duguet and Chris Pringle for finding exact solutions in the model. The authors would also like to thank an anonymous referee for suggesting the '$2+\epsilon$' nomenclature. This research was funded by the EPSRC under grant GR/S76144/01.

Appendix A. Boundary conditions

The Navier–Stokes equation (2.1) plus the boundary condition $\boldsymbol{u} = \boldsymbol{g}(\theta, z)$ are equivalent to (2.4) provided that on the boundary

$$\hat{\boldsymbol{n}} \cdot \nabla \wedge \left[\left(\partial_t - \frac{1}{Re} \nabla^2 \right) \boldsymbol{u} + \boldsymbol{b} \right] = 0, \tag{A 1}$$

where $\hat{\boldsymbol{n}}$ is its normal (see Marqués 1990). This condition ensures the term in the square brackets is equal to a gradient, such as the pressure. If not imposed, this term may be any $\chi \hat{\boldsymbol{z}}$, where $\nabla_h^2 \chi = 0$. If this is not a gradient, then an unknown body force is introduced. For the axisymmetric case χ is constant; the curl of $\chi \hat{\boldsymbol{z}}$ is then zero; and therefore the condition is redundant. Otherwise, from the diffusion term in (A 1), using the properties $\nabla^2 \boldsymbol{u} = -\nabla \wedge \nabla \wedge \boldsymbol{u}$ and $\nabla \wedge \nabla \wedge (\hat{\boldsymbol{z}} f) = \nabla(\partial_z f) - \hat{\boldsymbol{z}} \nabla^2 f$, one finds

$$\begin{aligned} \hat{\boldsymbol{r}} \cdot \nabla \wedge \nabla^2 \boldsymbol{u} &= \hat{\boldsymbol{r}} \cdot \nabla \wedge \nabla \wedge \left(\hat{\boldsymbol{z}} \nabla_h^2 \psi \right) + \hat{\boldsymbol{r}} \cdot \nabla \wedge \nabla \wedge \nabla \wedge \left(\hat{\boldsymbol{z}} \nabla_h^2 \phi \right) + \partial_{zz} \hat{\boldsymbol{r}} \cdot \nabla \wedge \boldsymbol{u} \\ &= \partial_{rz} \psi_1 - \frac{1}{r} \partial_\theta \phi_2 + \partial_{zz} \hat{\boldsymbol{r}} \cdot \nabla \wedge \boldsymbol{g}, \end{aligned}$$

which leads to the last condition of (2.5). The other conditions simply express $\boldsymbol{u} = \boldsymbol{g}(\theta, z)$ with the gauge freedom $\phi = 0$ on the boundary.

The simplified system for the axially averaged flow, $h(r, \theta)$, arises because there exists a closed circuit c that is not simply connected running along the axial direction. This has an associated condition

$$\int_c \left[\left(\partial_t - \frac{1}{Re} \nabla^2 \right) \boldsymbol{u} + \boldsymbol{b} \right] \cdot \mathrm{d}l = 0,$$

which together with P_z on the second curl of the Navier–Stokes equations leads to the governing equation for h. The boundary condition $h = 0$ assumes $P_z(g_z) = 0$, which otherwise would correspond to a translating pipe or moving frame.

Appendix B. Solution for coupled boundary conditions

Each Fourier mode for ψ, ϕ is expanded as the superposition

$$\begin{aligned} \psi(r) &= \bar{\psi}(r) + a\, \psi^H(r), \\ \phi(r) &= \bar{\phi}(r) + b\, \phi^H(r), \end{aligned} \tag{B 1}$$

where the coefficients a and b are scalars. Subscripts k and m have been dropped. The barred and superscripted functions solve two distinct systems. Firstly,

$$\left(\partial_t - \frac{1}{Re} \nabla^2 \right) \bar{\phi}_2 = -(1 - P_z)\, \hat{\boldsymbol{z}} \cdot \nabla \wedge \nabla \wedge \boldsymbol{b}, \tag{B 2}$$

$$\begin{aligned} \nabla^2 \bar{\phi}_1 &= \bar{\phi}_2, \\ \nabla_h^2 \bar{\phi} &= \bar{\phi}_1, \end{aligned}$$

$$\left(\partial_t - \frac{1}{Re} \nabla^2 \right) \bar{\psi}_1 = \hat{\boldsymbol{z}} \cdot \nabla \wedge \boldsymbol{b}, \tag{B 3}$$

$$\nabla_h^2 \bar{\psi} = \bar{\psi}_1,$$

with boundary conditions

$$\bar{\phi}_2 = \bar{\phi} = 0, \quad -\bar{\phi}_1 = g_z, \quad \partial_r \bar{\psi}_1 = 0, \quad \begin{cases} \bar{\psi} = 0 & \text{if } m = 0, \\ -\partial_r \bar{\psi} = g_\theta & \text{if } m \neq 0, \end{cases} \tag{B 4}$$

where $\nabla^2 \equiv (1/r)\partial_r + \partial_{rr} - m^2/r^2 - \alpha^2 k^2$ and $\nabla_h^2 \equiv (1/r)\partial_r + \partial_{rr} - m^2/r^2$. This time-dependent system is written in matrix–vector form, according to the time and radial discretization, then inverted sequentially for $\bar{\phi}_2 \to \bar{\phi}_1 \to \bar{\phi}$ and $\bar{\psi}_1 \to \bar{\psi}$. The second homogenized system is

$$\left(\partial_t - \frac{1}{Re} \nabla^2 \right) \phi_2^H = 0, \tag{B 5}$$

$$\begin{aligned} \nabla^2 \phi_1^H &= \phi_2^H, \\ \nabla_h^2 \phi^H &= \phi_1^H, \end{aligned}$$

$$\left(\partial_t - \frac{1}{Re} \nabla^2 \right) \psi_1^H = 0, \tag{B 6}$$

$$\nabla_h^2 \psi^H = \psi_1^H,$$

with boundary conditions

$$\phi_2^H = 1, \quad \phi_1^H = \phi^H = 0, \quad \partial_r \psi_1^H = 1, \quad \begin{cases} \psi^H = 0 & \text{if } m = 0, \\ \partial_r \psi^H = 0 & \text{if } m \neq 0. \end{cases} \tag{B 7}$$

As this system has no time-dependent $\boldsymbol{b}$, solutions with superscript H may be precomputed. The original boundary conditions on ϕ and ψ are satisfied upon reconstruction from the barred and superscripted variables. Two boundary conditions are satisfied by construction for all cases: as $\bar{\phi}$ and ϕ^H satisfy trivial boundary conditions, $\phi = \bar{\phi} + b\,\phi^H = 0$ on the boundary; similarly $-\phi_1 = g_z$ is satisfied automatically.

For axisymmetric modes, $m = 0$, the system is of lower order, as ψ always appears as $\partial_r \psi$, including in the boundary condition. The condition involving $\boldsymbol{b}$ is not required for this case (see Appendix A). The simplest solution is to add the boundary condition $\psi = 0$ so that we may invert for ψ for all modes. When $m = 0$ the remaining two boundary conditions which couple the potentials are satisfied by selecting scalars a and b according to the following evaluated on the boundary:

$$a = -(\partial_r \bar{\psi} + g_\theta)/\partial_r \psi^H, \quad b = -(\partial_{rz} \bar{\phi} - g_r)/\partial_{rz} \phi^H \quad \text{if } m = 0. \tag{B 8}$$

For non-axisymmetric modes, $m \neq 0$, the condition $-\partial_r \psi = g_\theta$ is satisfied automatically. The last two conditions are satisfied by solving the system for a and b evaluated on the boundary,

$$\begin{bmatrix} \frac{1}{r}\partial_\theta \psi^H & \partial_{rz} \phi^H \\ -\partial_{rz} \psi_1^H & \frac{1}{r}\partial_\theta \phi_2^H \end{bmatrix} \begin{bmatrix} a \\ b \end{bmatrix} = - \begin{bmatrix} \frac{1}{r}\,\partial_\theta \bar{\psi} + \partial_{rz} \bar{\phi} - g_r \\ Re\, \hat{\boldsymbol{r}} \cdot \nabla \wedge \boldsymbol{b} - \partial_{zz}\, \hat{\boldsymbol{r}} \cdot \nabla \wedge \boldsymbol{g} \end{bmatrix} \quad \text{if } m \neq 0. \tag{B 9}$$

As this only requires the inversion of a 2×2 matrix and as the H-functions are pre-computed, this is an inexpensive way to ensure all boundary conditions are simultaneously satisfied to machine precision.

REFERENCES

Barkley, D. & Tuckerman, L. S. 2007 Mean flow of turbulent–laminar patterns in plane couette flow. *J. Fluid Mech.* **576**, 109–137.

Barnes, D. R. & Kerswell, R. R. 2000 New results in rotating Hagen–Poiseuille flow. *J. Fluid Mech.* **417**, 103–126.

Bottin, S. & Chate, H. 1998 Statistical analysis of the transition to turbulence in plane Couette flow. *Eur. Phys. J.* B **6**, 143–155.

Darbyshire, A. G. & Mullin, T. 1995 Transition to turbulence in constant-flux pipe flow. *J. Fluid Mech.* **289**, 83–114.

Duggleby, A., Ball, K. S., Kenneth, S., Paul, M. R. & F., Fischer P. 2007 Dynamical eigenfunction decomposition of turbulent pipe flow. *J. Turbul.* **8**, 1–24.

Duguet, Y., Willis, A. P. & Kerswell, R. R. 2008 Transition in pipe flow: the saddle structure on the boundary of turbulence. *J. Fluid Mech.* **613**, 225–274.

Eggels, J. G. M., Unger, F., Weiss, M. H., Westerweel, J., Adrian, R. J., Friedrich, R. & Nieuwstadt, F. T. M. 1994 Fully developed turbulent pipe flow: a comparison between DNS and experiment. *J. Fluid Mech.* **268**, 175–209.

Faisst, H. & Eckhardt, B. 2003 Travelling waves in pipe flow. *Phys. Rev. Lett.* **91**, 224502.

Faisst, H. & Eckhardt, B. 2004 Sensitive dependence on initial conditions in transition to turbulence. *J. Fluid Mech.* **504**, 343–352.

Gilbrech, D. A. & Hale, J. C. 1965 Further results on the transition from laminar to turbulent flow. In *Developments in Mechanics* (ed. S. Ostrach & R. H. Scanlan), vol. 2, pp. 3–15. Pergamon.

Hamilton, J. M., Kim, J. & Waleffe, F. 1995 Regeneration mechanisms of near-wall turbulence structures. *J. Fluid Mech.* **287**, 317–348.

Hof, B., van Doorne, C. W. H., Westerweel, J., Nieuwstadt, F. T. M., Faisst, H., Eckhardt, B., Wedin, H., Kerswell, R. R. & Waleffe, F. 2004 Experimental observation of nonlinear traveling waves in turbulent pipe flow. *Science* **305**, 1594–1597.

Hof, B., Juel, A. & Mullin, T. 2003 Scaling of the turbulence transition threshold in a pipe. *Phys. Rev. Lett.* **91**, 244502.

Hof, B., Westerweel, J., Schneider, T. & Eckhardt, B. 2006 Finite lifetime of turbulence in shear flows. *Nature* **443**, 59.

Itano, T. & Toh, S. 2001 The dynamics of bursting process in wall turbulence. *J. Phys. Soc. Jpn.* **70**, 703–716.

Jiménez, J. & Moin, P. 1991 The mimimal flow unit in near-wall turbulence. *J. Fluid Mech.* **225**, 213–240.

Kerswell, R. R. 2005 Recent progress in understanding the transition to turbulence. *Nonlinearity* **18**, R17–R44.

Kerswell, R. R. & Tutty, O. R. 2007 Recurrence of travelling waves in transitional pipe flow. *J. Fluid Mech.* **584**, 69–102.

Lagha, M. & Manneville, P. 2007 Modelling transitional plane Couette flow. *Eur. Phys. J.* **58**, 433–447.

Landman, M. J. 1990*a* On the generation of helical waves in circular pipe flow. *Phys. Fluids* A **2**, 738–747.

Landman, M. J. 1990*b* Time-dependent helical waves in pipe flow. *J. Fluid Mech.* **221**, 289–310.

Mackrodt, P. A. 1976 Stability of Hagen–Poiseuille flow with superimposed rigid rotation. *J. Fluid Mech.* **73**, 153–164.

Marqués, F. 1990 On boundary conditions for velocity potentials in confined flows: application to Couette flow. *Phys. Fluids* A **2**, 729–737.

Mellibovsky, F. & Meseguer, A. 2006 The role of streamwise perturbations in pipe flow transition. *Phys. Fluids* **18**, 074104.

Mellibovsky, F. & Meseguer, A. 2007 Pipe flow dynamics on the critical threshold. In *Proceedings of the 15th Intl Couette–Taylor Workshop*. Le Havre, France.

Moehlis, J., Faisst, H. & Eckhardt, B. 2004 A low-dimensional model for turbulent shear flows. *New J. Phys.* **6**, 56.

Mullin, T. & Peixinho, J. 2006 Recent observations in the transition to turbulence in a pipe. In *Proceedings of the IUTAM Symposium on Laminar–Turbulent Transition,* Bangalore, India.

Patera, A. T. & Orszag, S. A. 1981 Finite-amplitude stability of axisymmetric pipe flow. *J. Fluid Mech.* **112**, 467–474.

Peixinho, J. & Mullin, T. 2006 Decay of turbulence in pipe flow. *Phys. Rev. Lett.* **96**, 094501.

Peixinho, J. & Mullin, T. 2007 Finite amplitude thresholds for transition in pipe flow. *J. Fluid Mech.* **582**, 169–178.

Pfenniger, W. 1961 Transition in the inlet length of tubes at high reynolds numbers. In *Boundary Layer and Flow Control* (ed. G. V. Lachman), pp. 970–980. Pergamon.

Pringle, C. C. T., Duguet, Y. & Kerswell, R. R. in press Highly-symmetric traveling waves in pipe flow. *Phil. Trans. R. Soc. Lond.* arXiv:0804.4854.

Pringle, C. C. T. & Kerswell, R. R. 2007 Asymmetric, helical, and mirror-symmetric traveling waves in pipe flow. *Phys. Rev. Lett.* **99**, 207450.

Schneider, T. M., Eckhardt, B. & Vollmer, J. 2007*a* Statistical analysis of coherent structures in transitional pipe flow. *Phys. Rev.* E **75**, 066313.

Schneider, T. M., Eckhardt, B. & Yorke, J. A. 2007*b* Turbulence transition and the edge of chaos in pipe flow. *Phys. Rev. Lett.* **99**, 034502.

Schneider, T. M., Gibson, J. F., Lagha, M., Lillo, F. De & Eckhardt, B. 2008 Laminar–turbulent boundary in plane Couette flow. *Phys. Rev.* E **78**, 037301.

Toh, S. & Itano, T. 2003 A periodic-like solution in channel flow. *J. Fluid Mech.* **481**, 67–76.

Toplosky, N. & Akylas, T. R. 1988 Nonlinear spiral waves in rotating pipe flow. *J. Fluid Mech.* **190**, 39–54.

Viswanath, D. 2007 The dynamics of transition to turbulence in plane couette flow. arXiv: physics/0701337.

Wang, J., Waleffe, F. & Gibson, F. 2007 Lower branch coherent states in shear flows. *Phys. Rev. Lett.* **98**, 204501.

Wedin, H. & Kerswell, R. R. 2004 Exact coherent structures in pipe flow: travelling wave solutions. *J. Fluid Mech.* **508**, 333–371.

Willis, A. P. & Kerswell, R. R. 2007*a* Critical behaviour in the relaminarisation of localised turbulence in pipe flow. *Phys. Rev. Lett.* **98**, 014501.

Willis, A. P. & Kerswell, R. R. 2007*b* Reply to comment on 'critical behaviour in the relaminarisation of localised turbulence in pipe flow'. arXiv:0707.2684.

Willis, A. P. & Kerswell, R. R. 2008 Coherent structures in local and global pipe turbulence. *Phys. Rev. Lett.* **100**, 124501.

Wygnanski, I. J. & Champagne, F. H. 1973 On transition in a pipe. Part 1. The origin of puffs and slugs and the flow in a turbulent slug. *J. Fluid Mech.* **59**, 281–351.